

Assessing the potential for liquid solvents from X-ray sources: considerations on bodies orbiting AGN

D. Rodener¹, M. Hausmann¹ and G. Hildenbrand¹

¹Kirchhoff-Institute for Physics, Heidelberg University, INF 227, 69117 Heidelberg, Germany.

Received XXX ; accepted XXX

ABSTRACT

Aims. We aim to establish a rough first prospect on the potential of certain biorelevant solvents (water, ammonia and methane) to be present in liquid form inside the uppermost few meters of several modelled surfaces (rocky and icy crusts of various compositions) of hypothetical bodies orbiting active galactic nuclei (AGN), and investigate under which constraints this might occur.

Methods. We adjust and average together X-ray spectra from a sample of 20 Type 1 Seyfert galaxies to calculate a mean snowline of the sample used. Based on this, we introduce variation of a hypothetical body's orbit across distances between 10% and 100% of the snowline radius, and calculate a sub-surface attenuation within four different model surface compositions for each. Surface compositions are based on lunar soil and solvent ices found in the milky way's circumnuclear region. We then use this as a continuous source term for a thermal model. Example bodies are systematically investigated with sizes between 1/30 and 20 earth radii. Further outlier variations are also considered (such as the case of bound rotation of the body) to end up with a perspective of solvent phases under a wide slew of many different conditions.

Results. We find that liquid solvents are possible under a multitude of parameters, with temperature being the main constraint to liquid water and body size as well as pressure being the main constraint to liquid methane and ammonia. We further find that these results, when adjusted for snowline distance, depend less on the energy output of the central source within the Seyfert Type 1 AGN than on other parameters, such as body sizes and solvent properties.

Key words. galaxies: active – galaxies: Seyfert – galaxies: nuclei – X-rays: galaxies – planets and satellites: surfaces – astrobiology

1. Introduction

We aim to investigate some of the factors that play into the potential of (and the process of detecting) life outside of earth's own biosphere. We do this using a rudimentary first look into constraints of the habitability regarding one of the most bizarre astrophysical environments imaginable: the circumnuclear regions of active galactic nuclei.

The pre-existing variety of research pertaining to energy sources and the formation of liquid environments was an important step for astrophysics, astrochemistry as well as astrobiology. However, the respective research of uncommon energy sources has so far not thoroughly and in depth touched upon the possibilities that the combination of sub-surface environments and high-energy radiation offer.

Considerations on habitability get exceedingly complex, encompassing a wealth of topics such as energy supply, mechanisms to gather, store, transport, and process said energy in biochemical form, or the way by which extraterrestrial organisms might shield themselves from harmful influences such as radiation or temperature extremes. As such, a comprehensive look at the habitability of the environments discussed here would go far beyond any reasonable scope. We focus on only one aspect of habitability that both seems to be the most prevalent in both standard and proposed exotic biologies and is expected to exist in great abundance in the universe: liquid solvents.

The solvents were chosen based on the following considerations: water goes almost without saying, as it is the key solvent for most life on earth and fulfills many important roles such

as providing a transportation medium to distribute molecules throughout the organism. Methane and ammonia are also important solvents for complex life on earth, and are furthermore proposed in some models for exotic biochemistries (Stevenson et al. 2015, Palmer et al. 2017, Rampelotto 2010) with liquid methane proven to exist on Saturn's moon titan (Stofan et al. 2007) and liquid ammonia being suspected to (Grasset et al. 2000). These promising findings, as well as the beneficial thermochemical impact of salt-mixtures on water (with $NaCl$ being the most common salt in water on earth and $CaCl_2$ showing the most beneficial impact), lead us to choose these five solvents for our investigation.

Regarding the AGN, this work will thusly focus mainly on radio-quiet ones as external energy sources with X-ray emissions strong enough for their radiation to mostly penetrate both otherwise optically thick circumnuclear material¹ and the upper regions of regolith on bodies in their vicinity (which encompasses several parsec for objects such as these). This coincides with a recent proposal of planetary formation in the snowline around Seyfert-type AGN (Wada et al. 2019), but despite this overlap, we want to avoid strict adherence to the planetary properties considered in that work to keep a broad perspective on this uncommon field and check a reasonably wide slew of possibilities. A graphic overview of the model is given in Fig. 1.

¹ similar to the reasoning behind using X-ray luminosity for snowline calculations (Wada et al. 2019, 2021)

Send offprint requests to: G. Hildenbrand

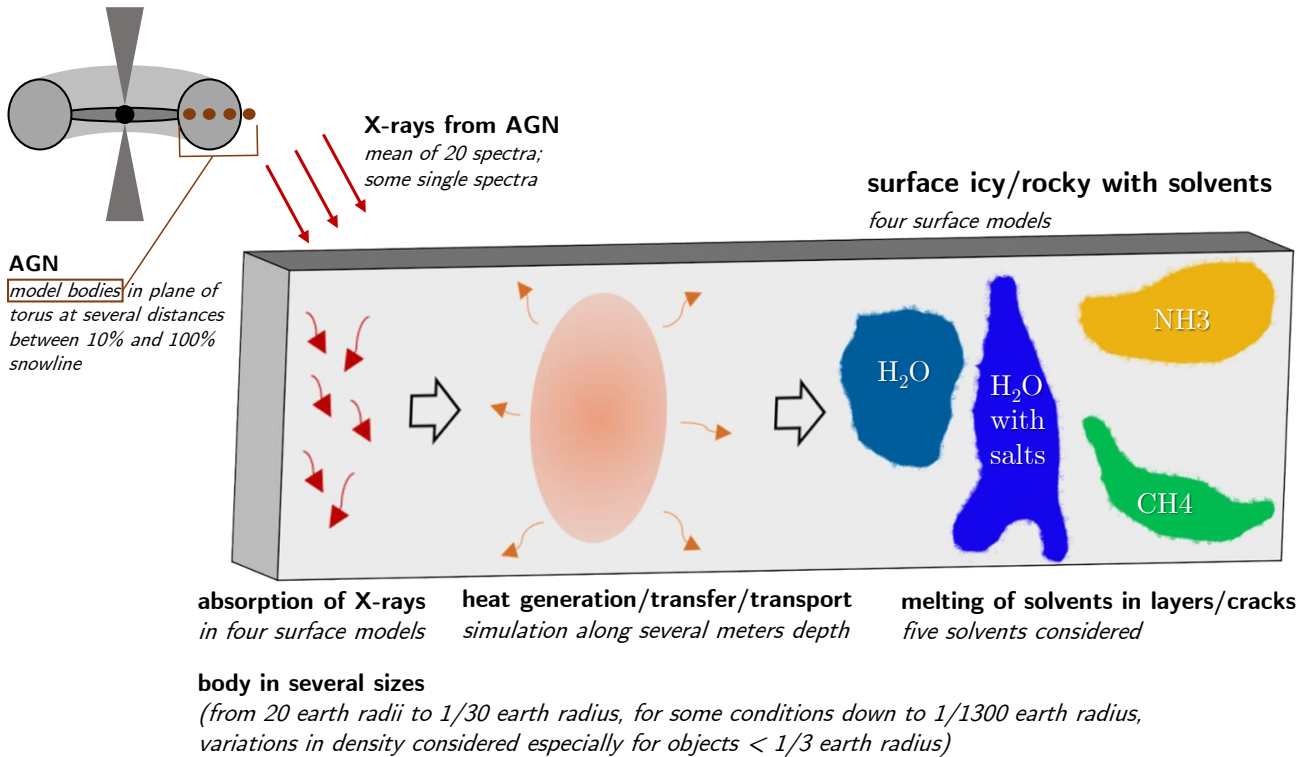


Fig. 1: Outline of the process behind this work: The mean of X-ray energy spectra of 20 individual AGN is used to compute energy absorption within five surface models.

2. Methods

2.1. Obtaining a mean energy spectrum

We sample 20 Type 1 Seyfert galaxies taken from a multi-wavelength catalogue of such objects. (Brown 2019)

Erroneous short dips into negative flux values observed in the data were interpreted as errors, likely of the detector, and were replaced with the value of the longer wavelength point adjacent to the sudden dip. Given the so-replaced values lie well within the bulk of the dataset, and that this was only necessary for a single spectrum, this solution was deemed satisfactory.

To obtain appropriate liquid layers in the subsurface, X-rays need to penetrate a non-negligible depth. We therefore focus on X-ray photon energies in the dataset between 1 and 120keV, as photons below 1keV do not penetrate very deep and the respective integrated flux does not generate enough heat to be of significance for the overall result of deeper liquid subsurface layers.

After having obtained such a spectra, a sketch of the modelling process is given in Fig. 1: The calculated absorbed energy is used as continuous source term for a thermal model calculating heat generation, transfer and transport down to a depth of 3 m, at the end of which a temperature profile is generated. This temperature profile is checked against the thermochemical properties of five model solvents (in combination with a value of pressure at different depths, calculated from 9 different body configurations) to determine where a given solvent could exist in the liquid phase.

2.1.1. Adjusting measurements for distance and angle

Using the distances (their calculation is outlined in Appendix A) for the observed targets from the point of observation (earth) R_{earth} , which were obtained using the astroquery python package (Ginsburg et al. 2019), as well as the flux received at this point of observation S_{earth} , we can determine the flux S_{model} received at a model planet at an orbit of radius r_{model} using the inverse square law to:

$$S_{model} = \frac{S_{earth}}{\left(\frac{r_{model}}{R_{earth}}\right)^2}, \quad (1)$$

However, this is first done for a distance of 10pc from the central source to establish a point at which we can calculate the mean of the taken sample.

Viewing angle is a more delicate issue. We can expect that most AGN show an incredibly large energy emission in pole-on direction (viewing the accretion disk from above) and only marginal energy emission in disk-on direction (Padovani 2017), however, we are unable to fully verify this as we are unable to observe a single such object from multiple angles. This is further complicated by a lack of precise information about the viewing angle at which we see these objects, as AGN are both too bright and too far away to resolve them sufficiently to make geometric assumptions about viewing angle, instead having to resort to using kinematics (Fischer et al. 2013) or similar derivation techniques. To combat these problems here, we use the assumption of a simple unified model of AGNs, which poses that different types of active galactic nuclei are all similar objects viewed at different angles and at different stages of a similar evolutionary process. (Antonucci 1993) According to this assumption then,

Seyfert 1 galaxies are viewed as pole-on, derived from the lack of broad emission lines that would be imbued in the spectrum by region of high-velocity dust and gas surrounding the accretion disk close to the equatorial plane.

However, a planet forming in the circumnuclear disk would not exist this high above the disk’s equatorial plane, it would be much more likely to form at a lower angle close to the denser regions of dust surrounding the AGN. To adjust for this in a sufficiently concise way, we utilize a formula expressing the reduction of observed apparent luminosity for a unified luminosity function for AGNs from (Zhang 2004), which expresses a reduction of the observed apparent luminosity by a factor of:

$$A_\theta = \cos \theta * \left(\frac{1 + 2 \cos \theta}{3} \right), \quad (2)$$

which then leads to a formula for the observed luminosity I'_λ :

$$I'_\lambda = I_\lambda * A_\theta, \quad (3)$$

where θ is the inclination angle of the accretion disk relative to the observer, with $\theta = 90^\circ$ for an edge-on view of the disk.

As the same work classifies Type 2 AGNs at an angle of 68° or greater, this angle would correspond to a position on the edge of the broad line region of the circumnuclear disk, and will therefore be used as an example value to set the model in.

2.1.2. Interpolating and Averaging

To effectively calculate a mean of the Seyfert galaxy sample, which all exhibit uneven datapoints, a universal grid is defined for the energy axis of the spectra that runs from the first to the last photon energy value that is in at least one of the spectral grids used. In this case this is between 1 and 120keV , defined with 5205 logarithmically equidistant steps. (The exact number arose from the construction of the framework.) This universal grid is then sliced corresponding to each of the contributing spectra, and each spectrum is in turn interpolated onto its respective slice. Interpolation is done using the “interp1d”-function of python’s “numpy”-package (Harris et al. 2020), set to also extrapolate missing values to circumvent conflicts at the boundaries. Values outside these boundaries (above and below a certain spectrum’s recorded range) are set to NaN. The result of this is an array of 20 spectra along a single x-axis.

After transposing, the mean can be calculated per energy value (in a kind of cross-section of the spectra) using numpy’s “nanmean”-function, which automatically disregards any NaN-values. This outputs a mean Seyfert 1 spectrum as it would be observed at a distance of 10 pc.

The distance at which this mean spectrum would exhibit a snowline is defined as the distance from the source where the equilibrium temperature of a body:

$$T_{eq} = \left(\frac{I_0(1 - A_B)}{4\sigma} \right)^{\frac{1}{4}}, \quad (4)$$

where I denotes the energy flux, A_B the surface albedo and σ is the Stefan-Boltzmann constant as obtained using python’s scipy package (Virtanen et al. 2020), becomes a set temperature, conventionally 170K . In this case, the X-ray albedo is almost zero and can be neglected, and we are interested at the flux at a certain distance $I(r_{snow}) = I_0$.

This snowline is calculated from the integrated flux of the mean spectrum (done using numpy’s trapezoid integration function `integrate.trapez`) to be at a distance of 11.45pc . Individual spectra as well as the averaged spectrum at 10pc and the latter also at the snowline of 11.45pc can be seen in Fig. 2.

Distance variation is introduced here with all following computations being done for a set of ten fractions (from 10% to 100%) of the snowline distance.

2.2. Obtaining surface properties for model bodies

With the radiation environment figured out, we construct models for potential bodies as well as their uppermost few meters of crust. We choose a series of body sizes between 20 and $\frac{1}{30}R_{earth}^2$ to systematically cover an array of possibilities, with two main anchor points: the factor 20 (although originally attributed to earth masses, not radii) stems from the planetary models proposed in (Wada et al. 2021), and radii down to $\frac{1}{30}R_{earth}$ act as an attempt in reaching sizes at which accretion energy and radioactive heating become less important, equivalent to asteroids or tiny moons in the solar system.

2.2.1. Proposing surface models

We lack chemical data about the circumnuclear disks (CNDs) of any Seyfert-type galaxy, and information about exoplanetary surfaces are extremely scarce as well.

To compensate for this, and build a reasonable initial model, we work with chemical composition and morphology similar to lunar soil as reported by (Alexander et al. 2016) to emulate rocky bodies and a pure solvent ice regolith to emulate icy bodies without many minerals in the upper layers, similar to icy moons found in the solar system. The former was based on multiple points of reasoning: the moon is the best-researched body without a significant atmosphere, we have extensive geological data about its surface regolith and the few exoplanetary surfaces we have data about have shown to be similar to the moon’s composition. (Kreidberg et al. 2019)

To introduce solvents to the originally dry lunar model, we propose the regolith porosity of 50% to be filled with (initially) solvent ices of water, methane, and ammonia. The ratio of these solvents, both when introduced to the lunar model and as part of the icy model, was determined – as a loose guideline – by the chemical abundances obtained from spectroscopic observations and models of the milky way’s own central region (Harada et al. 2015). Saltwater concentrations were chosen to yield maximum reduction of melting points. End results of the rocky crust filled with freshwater will be displayed in 4, while results for the other models will be elaborated upon in Appendix B.

In the interest of the scope of this work – and because minute details in the composition ultimately do not impact the mass attenuation coefficient a lot – we focus on the abundances of the relevant solvents, ignoring other volatiles with generally lower abundances such as CO or N_2 . The abundances of all molecules involved in our four models are shown in Table 1.

Another important factor (more important than even the input energy as shown in Fig. 3) is surface density. We approximate the overall complicated geometry of regolith by utilizing a calculated density from the density of compounds involved³ (and the porosity assumed), which can be seen in Table 2.

² For the bulk of the simulations. Special calculations with systems as small as $\frac{1}{1300}R_{earth}$ were done as well.

³ with data taken from the NIST WebBook (Linstrom 1997)

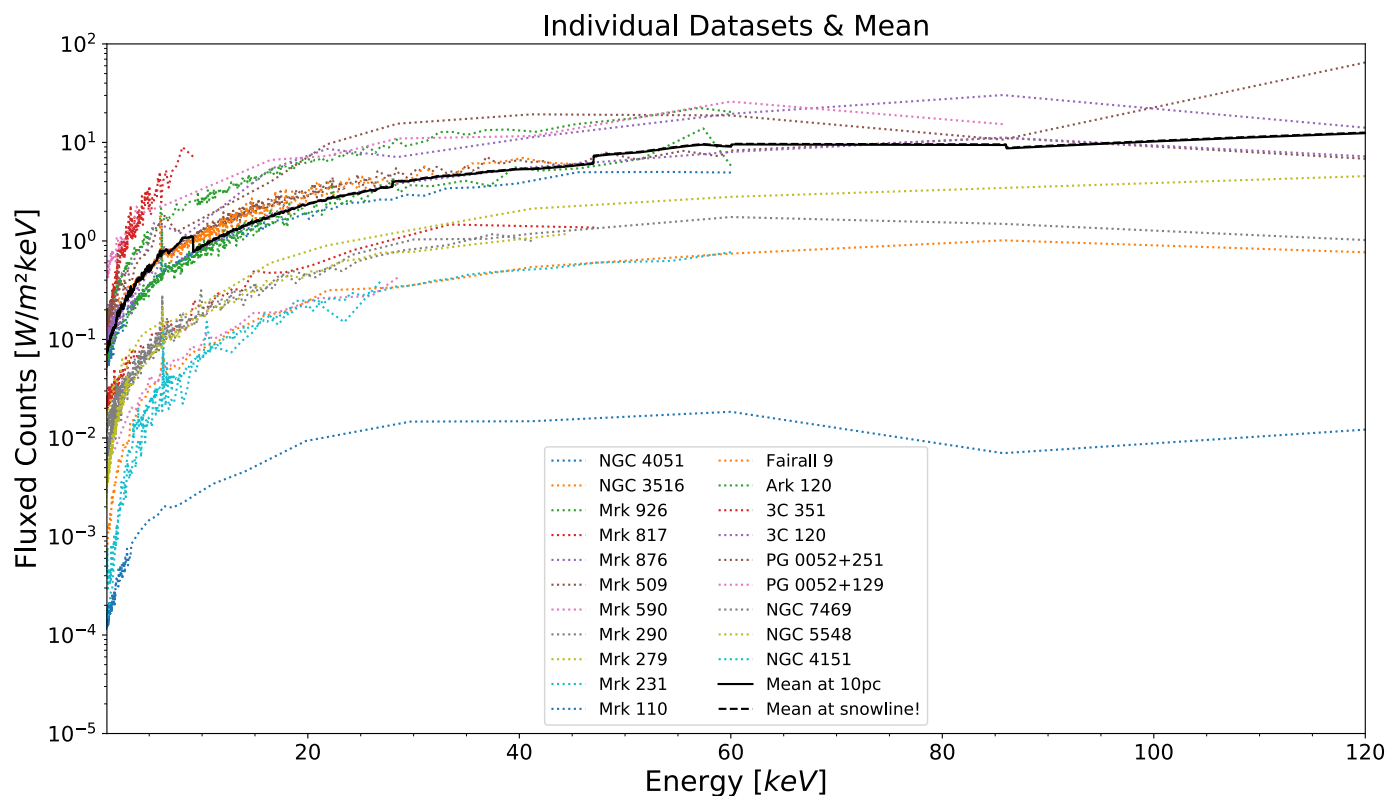


Fig. 2: Data of individual X-ray spectra based on the catalogue of (Brown 2019) (between 1 and 120 keV) of 20 Seyfert 1 AGNs used in this work (colored and dotted) as they would be observed at a distance of $10pc$, as well as a mean their spectra as it would be observed a distance of $10pc$ (black, solid line) and at a snowline distance of $11.45pc$ (black, dashed line).

Table 1: Surface compositions

Formula	Abundances			
	Icy Composition		Rocky Composition	
	Ice	Fresh ^a	$NaCl$ ^b	$CaCl_2$ ^c
H_2O	0.762	0.381	0.293	0.263
CH_4	0.17	0.085	0.085	0.085
NH_3	0.068	0.034	0.034	0.034
SiO_2		0.25	0.25	0.25
FeO		0.135	0.135	0.135
Al_2O_3		0.06	0.06	0.06
CaO		0.055	0.055	0.055
$NaCl$			0.088	
$CaCl_2$				0.118

^aLunar soil model with 50% solvent ices & fresh water

^bLunar soil model with 50% solvent ices & 23 wt% $NaCl$ -saltwater

^cLunar soil model with 50% solvent ices & 31 wt% $CaCl_2$ -saltwater

Table 2: Surface densities

Surface Model	Density [$\frac{g}{cm^3}$]
Rocky, freshwater	2.2765
Rocky, $NaCl$ -saltwater	2.3788
Rocky, $CaCl_2$ -saltwater	2.4121
Icy	0.8929

2.2.2. Calculating attenuated energy using Lambert-Beer's law

Attenuation in matter was calculated using Lambert-Beer's law in the form:

$$I_\lambda = I_{0,\lambda} \exp\left(-\frac{\mu}{\rho} \rho d\right), \quad (5)$$

where $I_{0,\lambda}$ and I_λ denote intensity respective before and after traversing a depth d inside matter of density ρ and with a mass attenuation coefficient of $\frac{\mu}{\rho}$. For the photon energies considered, the mass attenuation coefficient will vary with the photon energy. For this purpose, the mass attenuation coefficient of the investigated surface compositions has been obtained in an energy range between $1keV$ and $120keV$ using the national institute of standards and technology (NIST) XCOM database's online mass attenuation coefficient calculator for mixtures of molecules, which has in turn interpolated to fit onto the generalized energy grid constructed earlier. The result is shown in Appendix C.

This creates a family of spectral attenuation curves over both the energy and the depth grid. Integrating over the entire spectrum at each depth-point n allows us to obtain the bolometric intensity per depth, which, when subtracted from the intensity at a point $n - 1$, leads to information about the energy deposited inside the layer between n and $n - 1$ and thusly what amount of energy is available for heat generation⁴. This is shown in Fig. 3.

⁴ Only 90% of which will be used to generate the heat in this model however, with 10% being "reserved" for effects not inspected closer here such as secondary radiation and the modification of bonds of chemical compounds. This is discussed in detail in Appendix D.

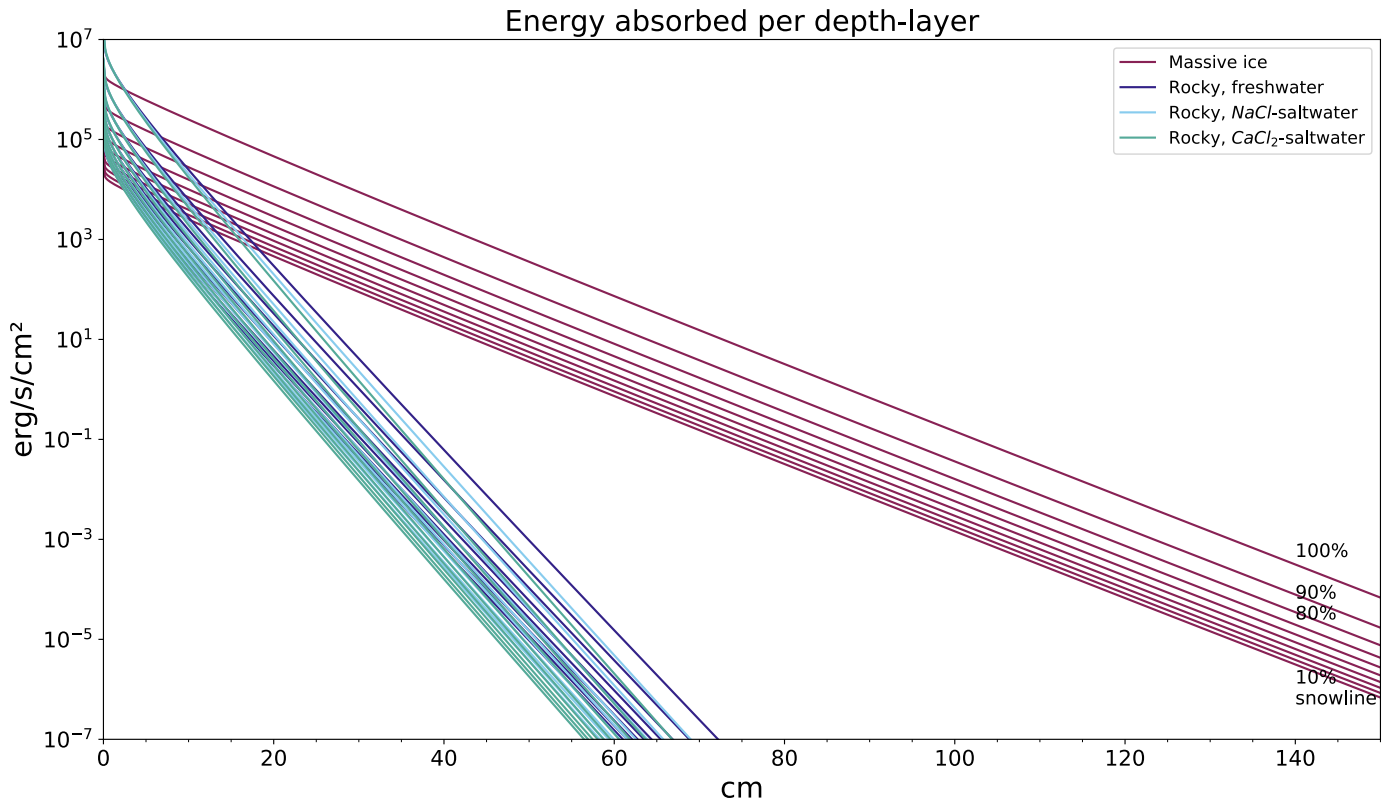


Fig. 3: Energy flux absorbed at a certain depth in 5 surface models, with a family of graphs from 10% to 100% snowline distance (descriptions of which are only shown for pure ice models for improved legibility in the graph), with different water-mixtures being very close to each other in the rocky model. What can be clearly seen is that salt water compositions have a small but noticeable impact on absorption, although the main determining factor of the absorption is material density.

2.2.3. Preparing thermal properties: Triple point depth

To determine whether a solvent is present in its liquid phase, the two key factors are temperature and pressure. Both of which are a complex matter which will need to be approximated to a certain degree, starting with pressure here. We obtained these pressures p_{triple} from the NIST Chemistry WebBook, NIST Standard Reference Database Number 69 (Linstrom 1997) and used them to calculate, for each model body, the depth at which the triple point would be reached, using:

$$d_{triple} = \frac{3p_{triple}}{4G\pi R_{body}\rho_{body}\rho_{surface}}, \quad (6)$$

whereas R_{body} and ρ_{body} denote the properties of the model body, that being a radius between 1/30 and 20 times earth's radius and a density equal to the overall average density of earth ($\rho_{body} = 5.51 \frac{g}{cm^3}$). $\rho_{surface}$ describes the density of the surface model as built in section 2.2.1. A detailed derivation of (6) is given in Appendix E.2.

2.2.4. Vapor pressure curve

The last step in determining the phase of a solvent, as mentioned in the previous section, is temperature, namely where a solvent reaches melting and boiling points. The melting point can be handled with relative ease, as most solvents show a constant melting point equalling the temperature at their triple point (anomalies notwithstanding). Triple point temperatures are discussed in detail in Appendix E.

To deal with the boiling point, we have access to multiple equations approximating part of the phase profile of certain substances, with a particularly simple and effective one being the Antoine equation:

$$\log_{10} p = A - \frac{B}{C + T}, \quad (7)$$

which relates the vapor pressure p with the respective boiling temperature T and a set of empirically determined coefficients A , B & C . This can be easily rearranged to determine the temperature instead of pressure with: $T = \frac{B}{A - \log_{10} p} - C$. Coefficients for freshwater, ammonia and methane were obtained from the NIST Chemistry WebBook, where we chose the sets with the widest temperature coverage, and can be seen in Table 3. The saltwaters saw adjustments in the form of shifting the equation by about four Kelvin along the T axis for both mixtures⁵.

2.3. Simulating thermal profile within the surface

2.3.1. Calculating specific heat capacities using polynomial equations

The goal is to arrive at a continuous temperature source term that can be fed to a numerical thermal model. For this purpose, we can compute temperature from the input energy derived earlier

⁵ corresponding to the boiling point shift of these mixtures at these concentrations

Table 3: Antoine coefficients of utilized solvents

Formula	Coefficients ^a		
	A	B	C
H_2O	1435.264	4.6543	-64.848
CH_4	443.028	3.9895	-0.49
NH_3	506.713	3.18757	-80.78

^aNIST Chemistry WebBook, NIST Standard Reference Database Number 69 (Linstrom 1997)

by using the specific heat capacity

$$c_p = \frac{1}{m} * \frac{dQ}{dT}, \quad (8)$$

which allows us to obtain the temperature change dT per timestep of a mass element m hit by a change in heat energy dQ , or in this case an amount of radiative energy I per timestep. We also introduce the conservative approximation that only roughly 90% of radiation hitting an average substance will be converted into heat, with the other 10% leading to secondary radiation effects not further discussed in this work. A detailed breakdown of the reasoning behind this can be found in Appendix D. Thus, to calculate the source term C we use:

$$C = dT = \frac{0.9 * dQ}{m * c_p} = \frac{0.9 * I}{V * \rho * c_p}, \quad (9)$$

splitting the mass element into volume V and density ρ . Density is carried over from the surface model constructed earlier, the radiation flux from the adjusted, meaned and integrated photometric data. The volume is chosen as a column of the height of one depth grid cell (0.1cm) over a unit area $1m^2$. This leaves the specific heat capacity to be determined.

Specific heat capacity: A popular way to account for temperature dependency of the specific heat capacity is the usage of the ‘‘Shomate equation’’, a polynomial equation that uses empirically determined coefficients A, B, C, D to approximate a c_p - T -curve. We used a slightly modified polynomial equation taken from the Chemical Engineering and Materials Research Information Center (CHERIC) database in the form of:

$$c_p = A + BT + CT^2 + DT^3, \quad (10)$$

with the result being in units of $\frac{kJ}{kg-molK}$. Noteworthy is that $kg-mol$ is a distinct unit equivalent to one kilomole, and thusly $\frac{kJ}{kg-molK} = \frac{J}{molK}$. This library, however, only encompasses values for liquids and gases, so solids need to be treated with exceptions:

a) Rocky solids: For most monoatomic solid materials of heavier atoms, the specific heat capacity is relatively constant, following the Dulong-Petit law (Landau & Lifshitz 1980):

$$c_p = 3R \approx 24.9 \frac{J}{molK}, \quad (11)$$

b) Ammonia ice & methane ice: For ammonia ice and methane ice, tables containing experimental information about the specific heat capacity can be found. For ammonia, this is Table IV in (Overstreet & Giauque 1937) which is used here up until 191 Kelvin, the melting point. For methane, Table 2 from (Yakub & Bodiul 2016) is used. In both cases, the so obtained data is fitted onto (10) using python’s SciPy package and a least

square fit. The polynomial coefficients obtained thusly are given over to the function calculating the overall specific heat capacity.

c) Water ice: For water ice, the specific heat is approximated using a different formula specific to it, as obtained from (Shulman 2004) in equation (1) of that work. It should be noted that this work outlines more precise ways to approximate ice’s specific heat (that is the main purpose of said paper), but for the scope of this work here, the lower precision formula given at the start is wholly sufficient:

$$c_p \approx 7.8 * 10^{-3} T \frac{J}{gK} * 18 \frac{g}{mol} = 0.1404 * T \frac{J}{molK}. \quad (12)$$

With the specific heat capacities obtained, a function was written to calculate the overall heat capacity of the mixture, depending on current temperature and pressure of the simulation, using the known abundances as a sum over all involved substances:

$$c_{p,tot} = \sum_i N_i * c_{p,i}. \quad (13)$$

2.3.2. Setting up a solver for the 1-D heat equation

The core of this thermal solver is the 1-D heat equation with advection and an additional continuous source term. A finite difference method to solve this problem numerically was described in (Riflet) based on a Forward Time Central Space (FTCS) scheme used to solve the 1-D heat equation with no source term. This method utilized the algorithm used to solve a 1-D heat equation with diffusivity and decay:

$$T_i^{*n+1} = Dif * T_{i+1}^n + (1 - k\Delta t - 2Dif)T_i^n + Dif * T_{i-1}^n. \quad (14)$$

Here, T describes the temperature, k is the decay coefficient which will be set to 0^6 and Δt is the width of steps within the discrete time grid used. In accordance with this, Δx describes the spacing of the space grid. Subscript indices (i) denote steps over the space grid, while superscript indices (n) denote time. Dif is the thermal diffusivity coefficient adjusted onto the space and time grid used, as:

$$Dif = \mu \frac{\Delta t}{\Delta x^2}, \quad (15)$$

with thermal diffusivity coefficient μ . Given the simplicity of this scheme, we set $\mu = \mu_{ice} \approx 1.02 \frac{mm^2}{s}$.

To now implement continuous emission, a source term c is added flat to all spatial grid points $i = p$ where the external heating applies:

$$T_i^{n+1} = T_i^{*n+1} \quad (16)$$

$$T_i^{n+1} = T_i^{*n+1} + C\Delta t \quad (17)$$

In our case, the source term is applied to all spatial grid points but varies over it. Within the code, this is expressed using Numpy arrays along the spatial grid for both T and C .

Furthermore, to implement a day-and-night cycle relatively easy, the source term was only applied every other time step.

⁶ We do not account for lateral thermal decay as we are building a 1-D model, and horizontal thermal decay only occurs at the surface, which is controlled here using the equilibrium temperature.

Compared to a simple one-half multiplier on the source term, this implementation allows for the model to cool down during the simulated night steps.

Boundary conditions: At the initial spatial grid point (the exact surface layer), we set the temperature to be equal to the equilibrium temperature given the radiation input at that point.

$$T_0^{n+1} = T_{eq}, \quad (18)$$

The equilibrium temperature is an accurate measure for surface temperatures of atmosphere-less bodies, hence why we deemed this boundary condition a sound assumption. Otherwise, heat conducted upwards within the model and reaching the surface would either build up indefinitely (due to the lack of any further conduction and decay) or decay too fast (were the decay term kept for this purpose).

At the initial time grid point (time 0) we set the entire temperature profile to be the equilibrium temperature of the radiation influx profile.

$$T_i^0 = T_{eq,i}, \quad (19)$$

This alone would not be an accurate thermal model, but it provides a sufficient starting point. As the simulation progresses, conductive effects will correct this initial outset quickly to a more realistic profile.

2.3.3. Forming a frame for the simulation with continuous input

The full function takes arguments for the surface model, body size, the grid spacing Δx and Δt as well as the full simulation timeframe *time*. With a given profile of absorbed energy calculated in section 2.2.2, the boundary conditions for the thermal solver are calculated and then applied to that solver recursively, meaning each timestep (T_i^n) provides the basis for the next timestep (T_i^{n+1}), over the length of a while loop running until a counting variable *t* reaches the full time *time*. A day-and-night cycle is simulated by setting up a boolean variable *day = True* before initializing the loop, and then using each loop step to flip the value using *day = not day*. The source term is only applied when *day = True*, thusly only ever other step.

Results are given to a dictionary. Said dictionary is plotted directly⁷ and, using temperature and pressure criteria discussed in section 2.2.3 and Appendix E, used to evaluate the phase of contributing solvents.

2.4. Notes about IPython multiprocessing for the simulation

The character of this work, with several simulations running over multiple, independent parameters, lends itself to multiprocessing, that is having multiple simulations run simultaneously on different CPU threads. For this purpose, computations have been done in the IPython environment (Perez & Granger 2007) and use its built-in multiprocessing package *ipyparallel* (IPython 2015). This allows us to execute certain cells of IPython notebooks on different clusters, using a multicore processor to its full extent while shortening overall computation time if multiple simulations are run simultaneously.

⁷ Calculations were done in separate clusters, but plotting was done in the general IPython environment. This necessitates extra steps at this point that are laid out in more detail in section 2.4.

With this arise some quirks: We ran all computations, with the exception of the final simulation, on all clusters to ensure all necessary variables were available in all clusters. The final plots were done in the general IPython environment (using the *matplotlib* python package (Hunter 2007)), and for this purpose results from the simulation as well as necessary variables from earlier parts of the code were transported from specific clusters to the general environment using *.push* and *.pull* commands of the *ipyparallel* package.

3. Results

The results displayed in Fig. 4 are a detailed breakdown of where, and under what conditions, the discussed solvents would be liquid given the rocky, “lunar soil” model with freshwater ices. (Results for the other surface models as well as some further conditions considered can be found in Appendix B.) The 9 sub-plots seen show the nine sizes of model bodies considered in this work, from largest at 20 earth radii to smallest at 1/30 earth radii - smaller sizes are discussed in Appendices F.3 and F.4. The y-axes display model depth beneath the surface, with the surface itself (depth 0) placed at the top of each sub-plot. The x-axes display groupings of the ten considered orbital distances between 10% and 100% $r_{snowline}$. Within each of these groupings, the five different solvents considered are displayed with different colors. As such, the bars display where solvents would be liquid and are labeled with the respective bar’s length (representing the thickness of the liquid layer), taking both the subterranean pressure and temperature into account. We can then make some key observations based on these results:

1. It is possible for solvents to be liquid on (and in) bodies orbiting an AGN at a few parsecs of distance, fueled entirely by the X-ray emission of that AGN. This can happen in a somewhat wide variety of environments, with the AGNs own energy output having much less of an impact compared to the density of a surface regolith (which greatly influences attenuation) or the size of the body itself (which greatly influences phase changes). The body’s inner density (beneath the regolith) plays a vital role as well, as seen in Appendix F.3. The influences are stronger for CH_4 and NH_3 .
2. Salt content of optimal concentration has an immensely beneficial effect on the thermal properties of water in extreme environments, and one can easily imagine that even away from the optimal concentration saltwater could beget liquidity on otherwise frozen worlds.
3. Unsurprisingly, different solvents are constrained by different variables in this simulation, depending on the respective thermal properties. Water’s main constraint is temperature: Freezing points determine if and at what distance from the central source liquid layers can form, while boiling points mainly determine how deep within the crust this has to happen. On bodies too close to the central source, water close to the surface evaporates (the consequences of which would lead to stark alterations in the model itself that have not been considered here, as it would be beyond the scope of this paper) while water too far below would not be warm enough to melt. Methane and ammonia are constrained mainly by pressure, which allows these substances to be liquid even close to the snowline if the pressure is sufficient - so if the body is large (and dense) enough.

To illustrate these key observations, we can determine that layers of liquid fresh water inside a rocky, lunar-like model with

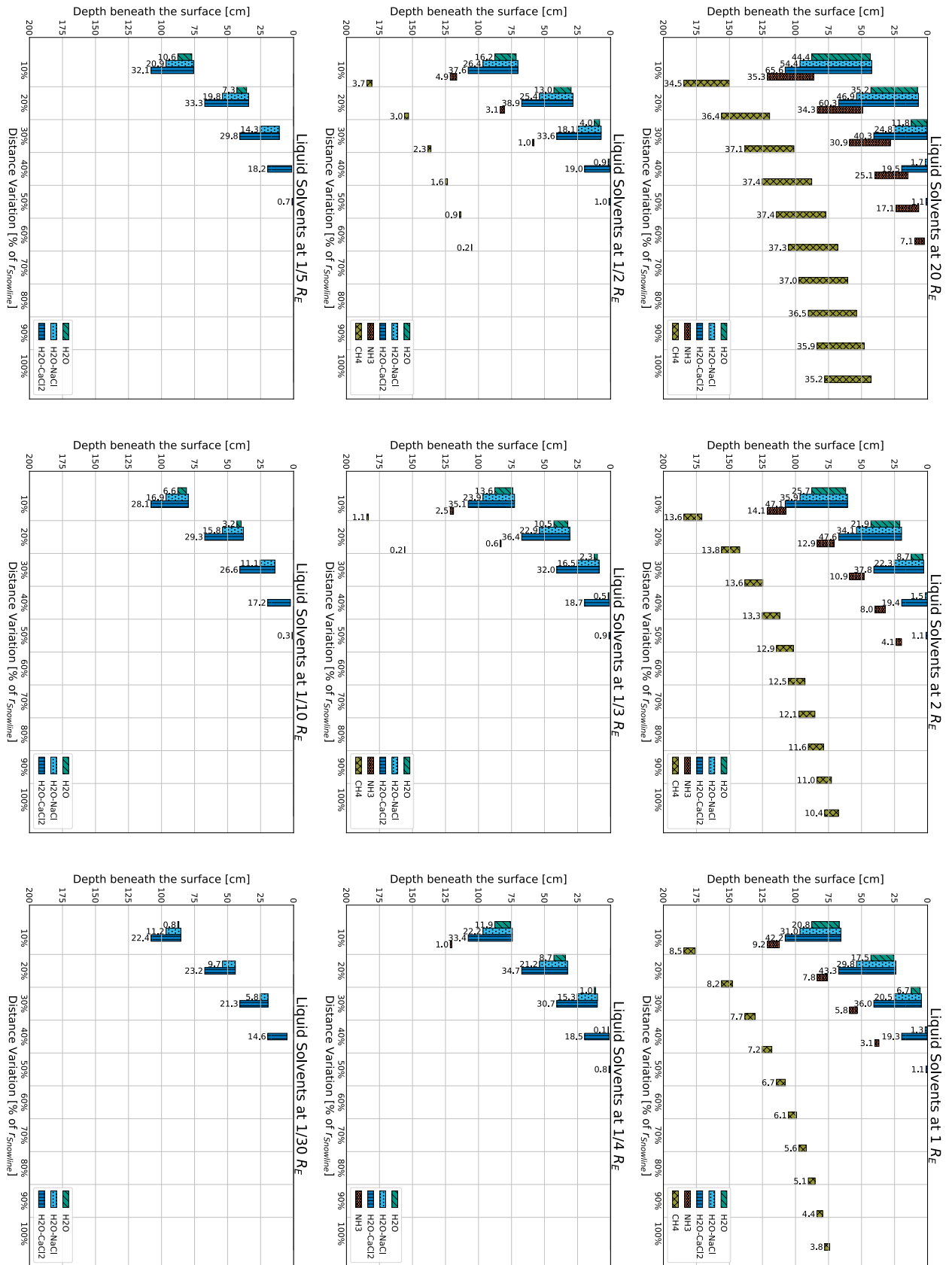


Fig. 4: Liquid solvent layers within the surface of 9 model bodies of rocky, freshwater surface composition around a modeled X-ray source. From top left to bottom right, the 9 bodies are of the sizes $20, 1, 2, \frac{1}{2}, \frac{1}{3}, \frac{1}{4}, \frac{1}{5}, \frac{1}{10}, \frac{1}{30} R_{\text{earth}}$ respectively. The surface density of the rocky, freshwater model involved is $\rho_{\text{surface}} = 2.2765 \frac{\text{g}}{\text{cm}^3}$, with the composition shown in Table 1. Numbers labelling the columns show the exact thickness of the liquid layers.

the largest thickness of 65 to 44cm would be found between 20 to $\frac{1}{5}R_{earth}$. Salt water behaves similarly, but can also form thick (up to roughly 65 cm) liquid layers on even smaller bodies down to $\frac{1}{30}R_{earth}$ thanks to the low triple point pressure (1mbar and 0.2mbar for optimal concentrations of NaCl- and CaCl₂-saltwater respectively, as opposed to 6.1mbar for freshwater).

The liquid layers may also be formed within bodies of lower densities (as shown in Fig. F.5) or much smaller radii down to just $\frac{1}{1250}R_{earth}$ (as shown in Fig. F.6) under certain conditions, especially for CaCl₂-saltwater.

A complete opposite behavior is seen within methane and ammonia: for those, triple point pressures are high, making them unable to exist in liquid form on bodies without a large radius in this model (and a high mass in general). However, on large enough bodies, methane and ammonia exhibit great versatility thanks to their temperature indifference. As such, methane can persist in liquid form on bodies at or above $\frac{1}{3}R_{earth}$ (but mostly if close to the AGN on the small bodies), and is able to cover the whole range of distances between 10 and 100% r_{snow} on bodies larger than $1R_{earth}$. Ammonia, while less versatile, can be liquid up to 60% snowline distance for $20R_{earth}$ and is able to form a slim layer at 10% r_{snow} on bodies the size of $\frac{1}{4}R_{earth}$. The details of other models and their respective constraints are expanded upon in the appendix.

Further variations of parameters and their influence on the stability of the liquid systems were investigated by considering both the daylight side of a possibly tidally locked body and limited the input to the two extremes of the AGN sample (the strongest and weakest non-outlier AGN). It can be shown that within the investigated group of AGN, there is little difference between strongest, weakest and the averaged spectra and the overall impact of the spectrum used as input is overshadowed by the greater impact of the chosen surface and body models. On the other hand, and as would be expected, the day-and-night cycle (and lack thereof) have a far larger impact of the temperature and subsequently liquid layers of solvents beneath a body's surface. A system without a day-and-night cycle generally pushes liquid layers further into the rock (however, we do not further inspect vaporization effects that might occur on the surface under higher temperatures, lending themselves to the formation of cryovolcanic activity) and allows for liquid layers on distances further from the central source, where liquid solvents were not possible on a rotating model. The detailed breakdown of this can be seen in Appendix F.

4. Discussion

Given the wide slew of parameters tested (different model body sizes, surface compositions and solvents considered), we consider it to be fairly certain that liquid solvents are possible on bodies in such an exotic environment as in an orbit around an active galactic nucleus. In the same vein, this wide slew of parameters together with the current lack of research on the topic does not allow a clear statement on the probabilities involved, which was, however, not the point of this work to begin with. It thus serves as a good base for further, even more complex, models.

One aspect to investigate in such future models may be the matter of crust stability. Several factors impact the stability of a celestial body's crust (present liquids, the presence and - if so - nature of an atmosphere and overall climate situation), and can do so in a drastic manner. Just in the solar system, we know the moon's regolith is stable enough for humans to comfortably walk

on, while some research has suggested the regolith of some icy moons such as Europa is so loose that it would be more akin to light, fresh snow than actual solid ground (Nelson et al. 2016). It would not be far from reason to also expect a complex interplay of solid, gas and liquid phase to result in unstable crusts in the form of cryovolcanism as expected on Titan (Mitri et al. 2008), especially in the models showing shallow water layers where eruption or refreezing events might lead to significant pressure buildup (while such a risk seems less significant for the often deeper layers of methane and ammonia). As a result of this, despite what the wider liquid layers found on larger model bodies might suggest, smaller model bodies are actually advantageous for the existence of liquid ammonia and methane. These volatiles would greatly destabilize the crust if too close to the surface, and smaller bodies (with therefore less gravity at play) necessitate any potential liquid layers to exist deeper beneath the surface, in turn stabilizing it indirectly. Even harsher conditions arise for models very close to the central source (at $\leq 20\% r_{snowline}$), as temperature profiles in these cases can be destructive (exceeding the melting points of rocky compounds), endangering the stability of even rocky crusts and necessarily needing evaporative effects of involved volatiles to be taken into account for a full assessment of the situation. As such, any results from 10% to 20% r_{snow} have to be investigated cautiously and should be reconsidered in new, more refined models. Similar considerations may be true for icy crusts close to the snowline. We also expect the rotation of a model body to play a large role, with the effects of a tidal lock having been shown here already. It can be expected that the opposite, a body with an anomalously high rotational velocity, would suffer problems of its own. These outliers would thusly be perfect candidates for exogeological and exoplanetary investigations of expectable surface composition and structure of a circumnuclear body.

This would also allow for more precise considerations on body size, a topic that has only been generally outlined in this work. While we find liquid methane and ammonia on bodies larger than half the radius of earth (equivalent to the Jovian moon Ganymede) at a depth of around 1 meter, liquid fresh and saltwater layers can effectively be found in bodies as small as $\frac{1}{30}R_{earth}$ (equivalent to the range of large asteroids such as Vesta), with both NaCl as well as CaCl₂ proving beneficial to a liquid phase. CaCl₂-saltwater alone may even be found in liquid layers on bodies ranging down to $\frac{1}{1250}R_{earth}$ (equivalent to the realm of comets under special conditions), as shown in Fig. F.6. On the other end of the scale, large bodies would pose their own set of challenges and interesting aspects that might influence these results, such as an accumulation of radioactive material and stored accretion energy begetting internal heating (similar to processes inside earth) or perhaps even the formation of gas giants under certain conditions.

On the topic of the aforementioned outliers, we lastly want to mention that especially the thermal buildup-effects (that result from hardcoding the equilibrium temperature at the outermost surface layer into the model), which can be seen in Appendix B, make it apparent that the thermal model employed here has very apparent limits. 2D heat transfer effects and, most notably, the tremendous impact of an atmosphere are also topic for further research. All of these open up possibility for an improved thermal model in future works.

These prospects about liquid solvents of course serve the greater purpose of enabling us to make educated considerations about the possibility of life in such exotic environments as seen here. Liquid layers of thicknesses between half a meter and a few millimeters seem unconventionally small biospheres, but simi-

lar microhabitats have already been considered on earth (Fritsen et al. 2001, Glass et al. 2021) and continue to grow in relevancy for astrobiology. This then warrants thoughts about the usability (and hostility) of the energy not just for the potential habitat itself, but the organisms within it as well. Models for the conversion of gamma-ray energy into biomass have already been proposed (Altair et al. 2018, Braun et al. 2016) before. But these models were developed for or from low energy environments, which makes it questionable if or how they may be applied to high energy environments, and applications of these models here would lead one to expect high, probably unrealistic amounts of potential biomass. Especially given that new restrictions on growth and homeostasis by the amount of gamma-radiation, the emergence and amount of secondary and tertiary particles, or potential new mechanisms for converting energy into useable units for living entities may play a bigger role. We would believe that a thoughtful analysis of the possibilities of gamma-ray driven life in this environment may deserve much deeper investigation, and as such consider that beyond the scope of this paper.

Our aim with this work was testing the waters (quite literally so) of a rather exotic, high-energy environment, and to add to the increasing awareness of the potential that circumnuclear clouds around active galactic nuclei hold. Our results show that solvents in such a model can exist in liquid phase even over a wide set of parameters. We thusly point to a number of new channels, especially in geology and astrobiology, for both in-depth theoretical work surrounding this and similar topics, as well as experimental investigations (such as remote sensing of appropriate sources or laboratory models of such environments) and deem our initial goal as successfully reached.

Acknowledgements. I would like to thank Malice Rudolph for aid in optimizing accessibility of the core figures in this work, as well as continued support concerning the English language.

References

- Alexander, L., Snape, J., Joy, K., Downes, H., & Crawford, I. 2016, *Meteoritics & Planetary Science*, 51
- Altair, T., de Avellar, M. G. B., Rodrigues, F., & Galante, D. 2018, *Scientific Reports*, 8, 260
- Antonucci, R. 1993, *Annual Review of Astronomy & Astrophysics*, 31, 473
- Bodnar, R. J. 2001, in *Lunar and Planetary Science Conference, Lunar and Planetary Science Conference*, 1689
- Braun, S., Morono, Y., Littmann, S., et al. 2016, *Frontiers in Microbiology*, 7, 1375
- Brown, M. 2019, *An Atlas of Active Galactic Nuclei Spectral Energy Distributions ("AGNSEDATLAS")*
- Carry, B. 2012, *Planetary and Space Science*, 73, 98
- CHERIC. 2011, *CHERIC Pure Component Properties*, accessed: 2021-10-23
- Fischer, T. C., Crenshaw, D. M., Kraemer, S. B., & Schmitt, H. R. 2013, *The Astrophysical Journal Supplement Series*, 209, 1
- Fritsen, C. H., Coale, S. L., Neenan, D. R., Gibson, A. H., & Garrison, D. L. 2001, *Annals of Glaciology*, 33, 280
- Ginsburg, A., Sipőcz, B. M., Brasseur, C. E., et al. 2019, *The Astronomical Journal*, 157, 98
- Glass, T. W., Breed, G. A., Iwahana, G., et al. 2021, *Ecology*, 102
- Grasset, O., Sotin, C., & Deschamps, F. 2000, *Planet. Space Sci.*, 48, 617
- Harada, N., Riquelme, D., Viti, S., et al. 2015, *Astronomy & Astrophysics*, 584, A102
- Harris, C. R., Millman, K. J., van der Walt, S. J., et al. 2020, *Nature*, 585, "357
- Hunter, J. D. 2007, *Computing in Science Engineering*, 9, 90
- IPython. 2015, *ipyparallel*
- Ketcham, S. A., Minsk, L. D., Blackburn, R. R., & Fleege, E. J. 1996, *Manual of practice for an effective anti-icing program*
- Khetan, Nandita, Izzo, Luca, Branchesi, Marica, et al. 2021, *Astronomy & Astrophysics*, 647, A72
- King, T. V. V., Clark, R. N., Calvin, W. M., Sherman, D. M., & Brown, R. H. 1992, *Science*, 255, 1551
- Kreidberg, L., Koll, D. D. B., Morley, C., et al. 2019, 573, 87
- Landau & Lifshitz. 1980, *Statistical Physics Pt. 1.* (Oxford: Pergamon Press), "193–196"
- Linstrom, P. 1997, *NIST Chemistry WebBook, NIST Standard Reference Database 69*
- Mitri, G., Showman, A., Lunine, J., & Lopes, R. 2008, *AGU Fall Meeting Abstracts*
- Nelson, R. M., Boryta, M. D., Hapke, B. W., et al. 2016, in *AGU Fall Meeting Abstracts*, P11C–1870
- Opatry, T., Richterek, L., & Bakala, P. 2016, *American Journal of Physics*, 85, 14
- Overstreet, R. & Giaque, W. F. 1937, *Journal of the American Chemical Society*, 59, 254
- Padovani, P. 2017, *Frontiers in Astronomy and Space Sciences*, 4, 35
- Palmer, M. Y., Cordiner, M. A., Nixon, C. A., et al. 2017, *Science advances*, 3, e1700022, 28782019[pmid]
- Perez, F. & Granger, B. E. 2007, *Computing in Science Engineering*, 9, 21
- Rampelotto, H. P. 2010, *Journal of Cosmology*, 5, 818
- Riflet, G. 2010
- Seltzer, S. 1995, *Tables of X-Ray Mass Attenuation Coefficients and Mass Energy-Absorption Coefficients, NIST Standard Reference Database 126*
- Seltzer, S. 2010, *XCOM-Photon Cross Sections Database, NIST Standard Reference Database 8*
- Showman, A. P. & Malhotra, R. 1999, *Science*, 286, 77
- Shulman. 2004, *Astronomy & Astrophysics*, 416, 187
- Stevenson, J., Lunine, J., & Clancy, P. 2015, *Science advances*, 1, e1400067, 26601130[pmid]
- Stofan, E. R., Elachi, C., Lunine, J. I., et al. 2007, *Nature*, 445, 61
- Virtanen, P., Gommers, R., Oliphant, T. E., et al. 2020, *Nature Methods*, 17, 261
- Wada, K., Tsukamoto, Y., & Kokubo, E. 2019, 886, 107
- Wada, K., Tsukamoto, Y., & Kokubo, E. 2021, 909, 96
- Williams, D. 2020, *Earth Fact Sheet*, <https://nssdc.gsfc.nasa.gov/planetary/factsheet/earthfact.html>, accessed: 2021-4-12
- XCOM. 2010, *NIST XCOM Selection*, accessed: 2021-10-23
- Yakub, L. & Bodiul, O. 2016, *Refrigeration Engineering and Technology*, 52
- Zhang, S. N. 2004, *The Astrophysical Journal*, 618, "L79"

Appendix A: Obtaining distances to investigated AGNs using astroquery and SIMBAD

To determine the flux arriving at a model planet located a certain distance from the central object, we first need to correct measurements taken for distance and viewing angle from both the measurements and the model planet in relation to the object's geometry. To apply the former using the inverse square law as will be shown in (1) we need distances from earth to the different galaxies of the sample.

Where possible for each of these objects, a direct luminosity distance was obtained from the SIMBAD online library. Where this was not possible, a redshift z was still available from SIMBAD and as a consequence the estimated distance D was approximated using Hubble's law:

$$D \approx \frac{cz}{H_0}, \quad (\text{A.1})$$

with c being the velocity of light in vacuum, and using a hubble parameter of $H_0 = 69.9 \frac{km}{s.Mpc}$ (Khetan, Nandita et al. 2021).

Accessing SIMBAD was done via the astroquery python package (Ginsburg et al. 2019), specifically astroquery.simbad, and setting up a custom query using object denominators taken from the filenames of (Brown 2019)-data.

Appendix B: Exhaustive model simulations and temperature curves

The main product of the actual thermal simulation is a temperature profile of the subsurface environment considered, as they precede the liquid layers determined as shown in section 3.

To keep the main part of this work focused, we show these temperature profiles here, alongside outcomes of the previously mentioned additional models, in Fig. B.2 (apart from the main model pertaining a rocky, freshwater-filled crust, the temperature profile of which can be seen in Fig. B.1).

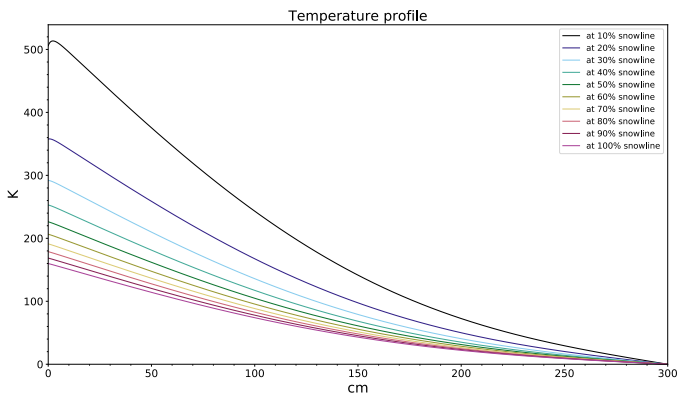


Fig. B.1: Temperature profile for the simulation using a rocky crust with freshwater inclusions.

Appendix C: Mass attenuation coefficient

The mass attenuation coefficients for the considered surface compositions, interpolated from data obtained from the NIST XCOM database as in explained in Section 2.2.2 is shown in Fig. C.1.

Appendix D: About heat conversion

As mentioned, when radiation hits a material not all of the energy is converted purely into heat with some energy resulting in secondary radiation or the chemical "upgrade" (breaking and reformation of chemical bonds, resulting in new compounds with the potential to store more energy than before) of the matter hit by radiation. While these secondary processes lie beyond the scope of this work, we wish to make a conservative estimation on the amount of photon energy that actually gets converted into heat to adjust the thermal model therewith.

This estimation is based on evaluating the amount of "pure" kinetic energy released in the medium as minimum input for heating (secondary and tertiary particles will also still render part of their energy into heat). This was done utilizing the mass energy-absorption coefficient $\frac{\mu_{en}}{\rho}$, which expresses the amount of energy from the incident photon that is transferred as kinetic energy to charged particles in the interaction minus the energy from photons resulting from the movement of these charged particles. When compared to the mass attenuation coefficient $\frac{\mu}{\rho}$, this lets us estimate the portion of attenuated energy "lost" to heating.

For a variety of substances (comparable to the compounds involved in our model, as no exact data for those could be obtained), in the energy range with the most impact from the analysed AGN spectra (50 keV to 150 keV) and for densities $\rho = 1 \frac{g}{cm^3}$ more than 80% and less than 90% of energy is absorbed via the mechanisms considered under $\frac{\mu_{en}}{\rho}$ (see Table D.1). At higher densities as they would be seen in the rocky compositions, absorption reaches more than 90% across the board.

This further encourages us to choose 0,9 as a very conservative factor, posing a general minimum of energy available to the thermal model."

Table D.1: Mass energy absorption and mass attenuation coefficients.

Substance	$E [keV]$				
	50	60	80	100	150
for $\rho = 1 \frac{g}{cm^3}$					
$\exp(\frac{\mu_{en}}{\rho} - \frac{\mu}{\rho}) [\%]$					
water, liquid	83.14	84.03	85.41	86.48	88.44
glass	83.64	84.77	86.36	87.49	89.44
concrete	83.12	84.33	85.99	87.17	89.17
for $\rho = 2 \frac{g}{cm^3}$					
water, liquid	91.18	91.67	92.42	93.00	94.04
glass	91.45	92.07	92.93	93.54	94.57
concrete	91.17	91.83	92.73	93.36	94.43
for $\rho = 3 \frac{g}{cm^3}$					
water, liquid	94.03	94.36	94.88	95.27	95.99
glass	94.22	94.64	95.23	95.64	96.35
concrete	94.02	94.48	95.09	95.53	96.25

A list of mass energy absorption coefficient $\frac{\mu_{en}}{\rho}$ values, mass attenuation coefficient $\frac{\mu}{\rho}$ values, both from (Seltzer 1995), and the portion of attenuated energy NOT lost in secondary processes $\exp(\frac{\mu_{en}}{\rho} - \frac{\mu}{\rho})$.

Appendix E: About the triple point (equivalent)

Appendix E.1: Triple point (equivalent) properties

The properties for fresh water, methane and ammonia have been obtained from a NIST database. The matter gets more complicated when dealing with saltwater however, it can be shown (Bodnar 2001), that the triple point equivalent⁸ of saltwater solu-

⁸ Triple points are strictly speaking only defined for pure substances, we here use the critical point equivalent of a triple point as we are not

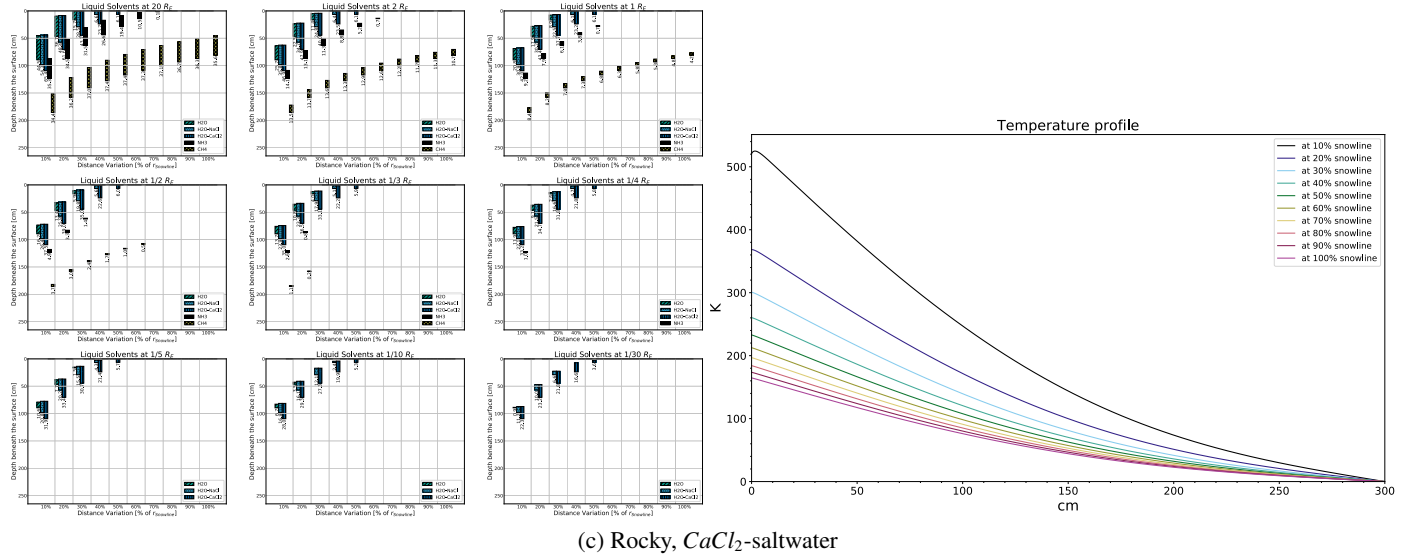
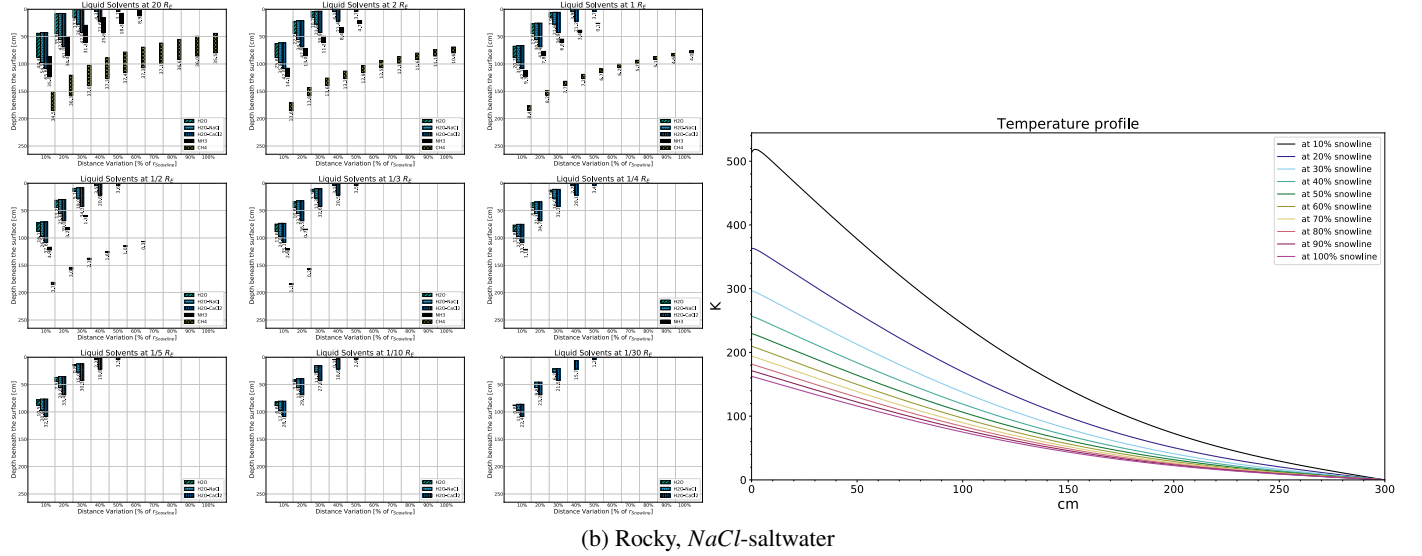
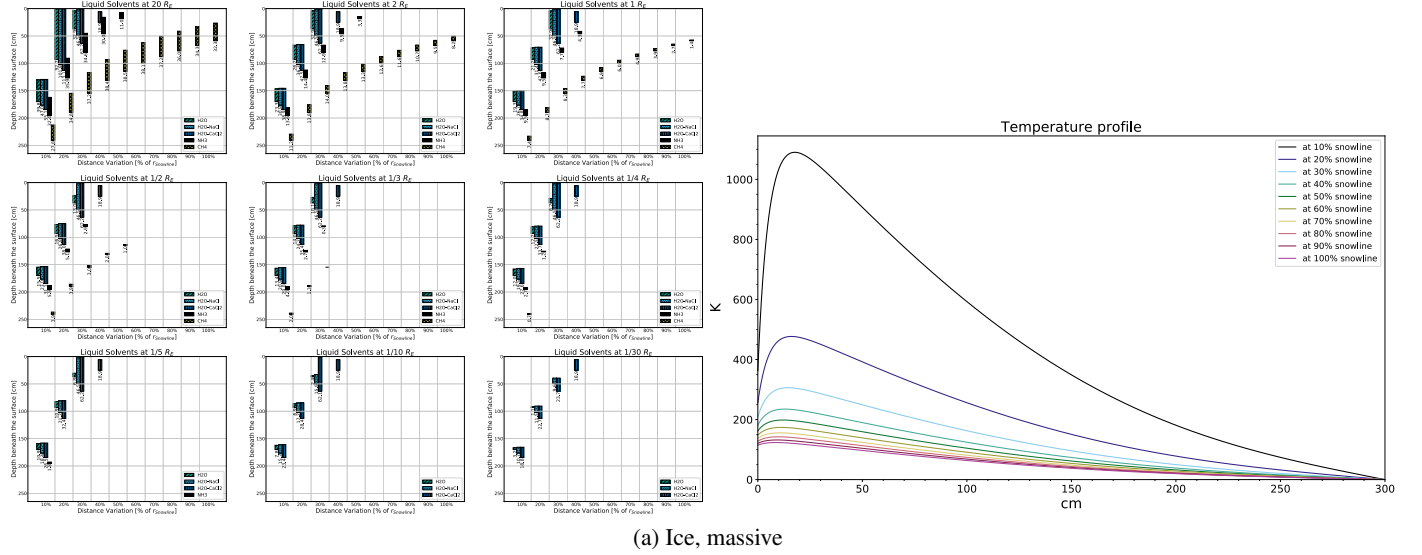


Fig. B.2: Simulations for the three exhaustive simulations of rocky crust with NaCl-saltwater inclusions, rocky crust with CaCl₂-saltwater inclusions and icy crust

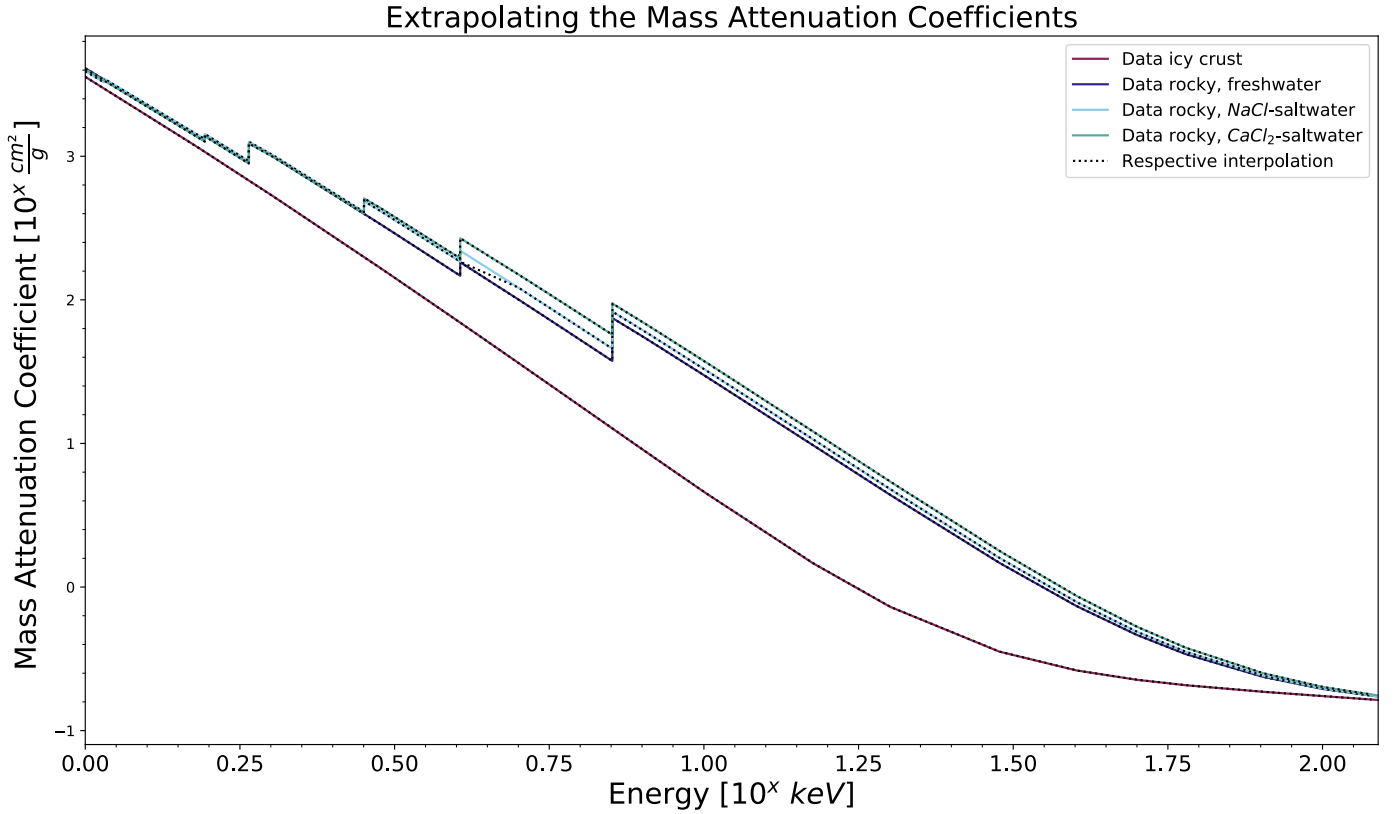


Fig. C.1: Mass attenuation coefficient for four surface compositions.

tions at their eutectic points can be approximated by the vapour pressure of pure water ice at that temperature. So, using the known temperatures of the eutectic points of $NaCl$ -Saltwater at 23wt% and $CaCl_2$ -Saltwater at 30wt% (Ketcham et al. 1996) we can determine the respective equivalent for the triple point pressure from the behavior of fresh water. All resulting triple point (equivalents) are shown in Table E.1.

Table E.1: Triple point (equivalent) properties

Formula	Properties	
	p_{triple} [bar]	T_{triple} [Kelvin]
H_2O	0.0061 ^a	273 ^a
CH_4	0.117 ^a	91 ^a
NH_3	0.061 ^a	195 ^a
$NaCl$	0.001 ^b	252 ^b
$CaCl_2$	0.0002 ^b	223 ^b

^aNIST Chemistry WebBook, NIST Standard Reference Database Number 69 (Linstrom 1997)

^bKetcham et al. 1996

Appendix E.2: Derivation of triple point depth

In equation (6) the depth at which the triple point pressure, that is the pressure necessary for the relevant solvents to melt (instead of just sublimate), is calculated. The process of arriving at this equation is outlined here:

The triple point pressure p_{triple} is a material constant and can be obtained from databases or literature, and can be expressed as the gravitative force F_g of (on an atmosphereless body: just) the

interested in the exact phase behavior, merely the minimum pressure and temperature necessary for liquids to occur.

ground above an observed area A , which here lies at the desired depth d_{triple} :

$$p_{triple} = \frac{F_g}{A}, \quad (E.1)$$

The force can then be broken down, where in this case m_{body} denotes the mass of the planet below the area at d_{triple} and $m_{surface}$ denotes the mass of the crust weighing down from above:

$$F_g = G \frac{m_{body} m_{surface}}{r^2}, \quad (E.2)$$

Since we later want to vary the object radius R_{body} of hypothetical bodies, but not their density ρ_{body} , which we set to $\rho_{body} = \rho_{earth,mean} = 5.51 \frac{g}{cm^3}$ (Williams 2020), to simplify the model, it is a good choice to further break down:

$$m_{body} = V_{body} \rho_{body} = \frac{4}{3} \pi R_{body}^3 \rho_{body}, \quad (E.3)$$

$$m_{surface} = V_{surface} \rho_{surface} = A d_{triple} \rho_{surface}, \quad (E.4)$$

As our model in general only considers depths of up to 3 meters, it is neglectable when compared to the radius of all the considered models (between 20 and $\frac{1}{30} R_{earth}$) so the radius in (E.2) can be assumed to be equal to R_{body} . As such, we can insert (E.4) and (E.3) into (E.2) and this then into (E.1) and simplify:

$$p_{triple} = \frac{1}{A} G \frac{\frac{4}{3} \pi R_{body}^3 \rho_{body} A d_{triple} \rho_{surface}}{R^2} \quad (E.5)$$

$$= G \frac{4}{3} \pi R_{body} \rho_{body} d_{triple} \rho_{surface}, \quad (E.6)$$

which we can rearrange to reach our desired equation (6) for the triple depth.

Appendix F: Further variabilities investigated

As a final step, we consider two points of variability not touched upon before: one is the impact of AGN-flux, and by extension the mean done to simplify calculations here, on temperature curve and liquidity of solvents. The other is the impact of the implemented day-and-night-cycle on the results.

Appendix F.1: Simulation on a tidally locked body

For this, we disable the part of the code that ensures the continuous source term is added only every other timestep, simulating the lit side of a body tidally locked to the AGN. (Terminator results are not simulated, rotation is generally half the stepping.) While it should be noted that tidal locking seems unlikely for bodies orbiting several parsecs away from the source (even if said source is supermassive), it allows us to investigate an extreme case. This will be especially interesting in potential follow-up work considered atmospheric bodies. Results, as can be seen in Fig. F.2b) for the rocky freshwater model, while not extremely different to the normal simulation (which is shown, with adapted scales, in Fig. F.1), show obvious distinctions, especially that a “tidally locked” model allows liquid layers where none were possible on a rotating body, most notably ammonia on bodies as small as $\frac{1}{5}R_{earth}$ if close enough to the source, or methane on bodies as far away from the source as 40% r_{snow} on bodies the size of $\frac{1}{5}R_{earth}$.

Appendix F.2: Simulation with individual galaxies

To compare the different impacts that strong and weak sources have on the eventual results, two runs of the simulation were performed not using the input of the averaged spectrum of all 20 AGN, but instead spectra of two non-averaged, individual AGN. Specifically NGC 3516 and Mrk 876, which were identified as strongest and weakest non-outlier source of the dataset respectively. The results, as can be seen in Fig. F.3 and F.4, differ only barely from that of the averaged spectrum used for the main simulation, which confirms that in this simulation, the strength of the source (as long as said source is of the same, Seyfert 1, object class) has only marginal impact on the temperature profile resulting from them.

What can also be seen is that counterintuitively, not only does the weaker AGN result in wider liquid layers than the stronger one, but both are outdone by the meaned input. The key factor at play here is the spectrum’s shape, namely their comparative flux at the highest energies investigated. When normed for the same integrated flux (which is the case for the flux at snow-line), Mrk 876 contributes less high-energy radiation compared to NGC 3516 (and both less compared to the meaned spectrum), and as a result less radiation penetrates as deeply and liquid layers are (ever so slightly) slimmer.

Appendix F.3: Simulations of small moons and asteroids

We then did rough approximations of four small real bodies in the solar system to show the results of a more constraint but realistic approach to density and size. Simulations were ran after adjusting ρ_{body} (as mentioned in E.2) to the density of Ganymede ($1.936 \frac{g}{cm^3}$), 511 Davida ($2.48 \frac{g}{cm^3}$), Europa ($3.014 \frac{g}{cm^3}$) and 4 Vesta ($3.58 \frac{g}{cm^3}$) (Showman & Malhotra 1999, Carry 2012) respectively. We further modified crust density to be equal the body density for the asteroid 511 Davida, as it is non-differentiated. Results are shown in Fig. F.5.

Appendix F.4: Determining the minimum valid model body size

As a last point of this appendix, we attempt to determine a rough measure of how small a body within a certain subset of parameters must be in order to support any form of liquid layers. This has been done by manually adjusting the model body sizes within the final calculations of where liquid layers are present using the thermal profile of the rocky crust model as an input - meaning that these different sizes were not taken into account during the simulation of said thermal profiles, again to stay within a certain realistic scope. The results can be seen in Fig. F.6. One can see that, in accordance with our previous assessments, saltwater is able to persist with only marginal limitations from a body’s size (and therefore the pressure environment beneath the surface). This results in $CaCl_2$ -saltwater’s ability to, in our simulations, stay liquid even on bodies as small as $\frac{1}{1250}R_E \approx 5km^9$. It should be noted that at this size, many other factors may support or hamper the persistence of liquid solvents that we did not take into account here, but this serves as a fitting proof-of-concept that, in environments such as the ones considered here, even bodies as small as this are worth investigating more closely.

⁹ We consider the visible sub-millimeter remnant at $\frac{1}{1275}R_E$ practically unviable and a potential artifact of the simulation, due to it being smaller than the respective stepsize.

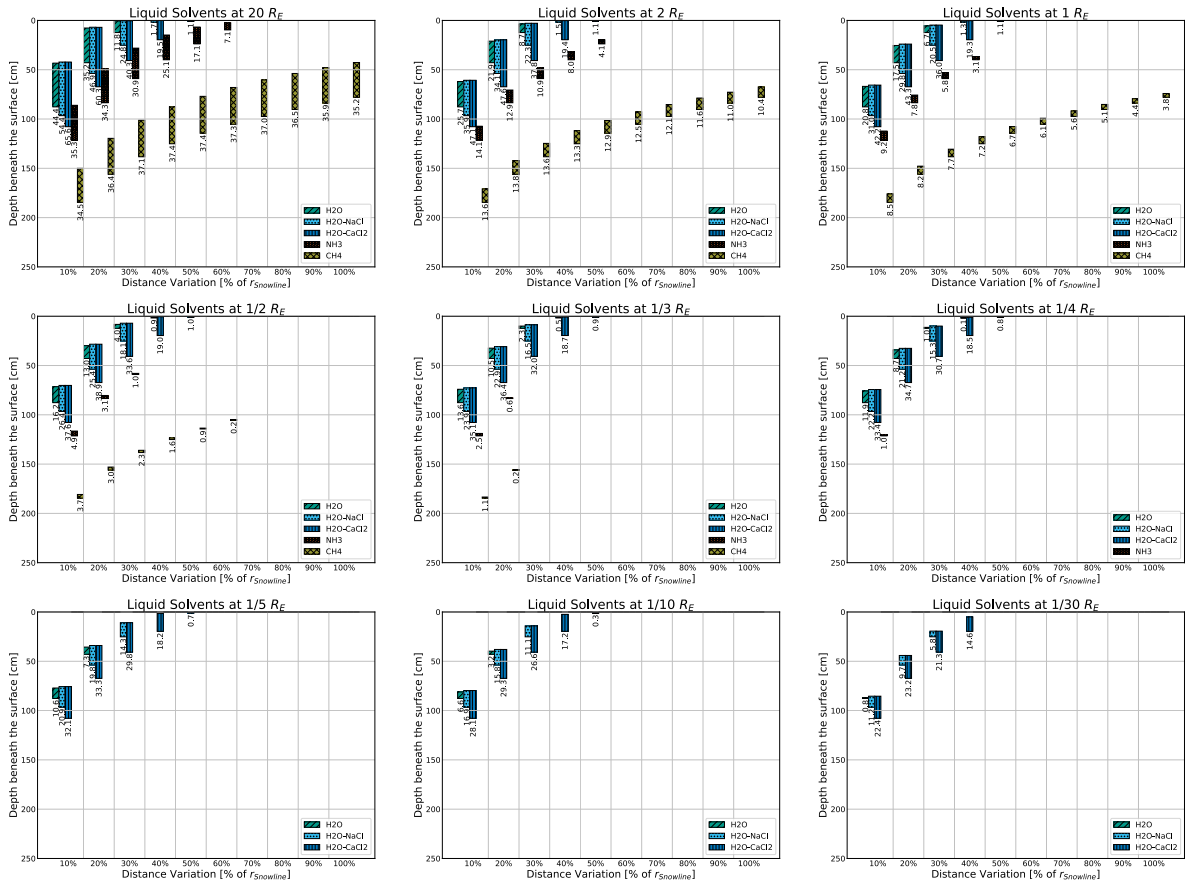


Fig. F.1:

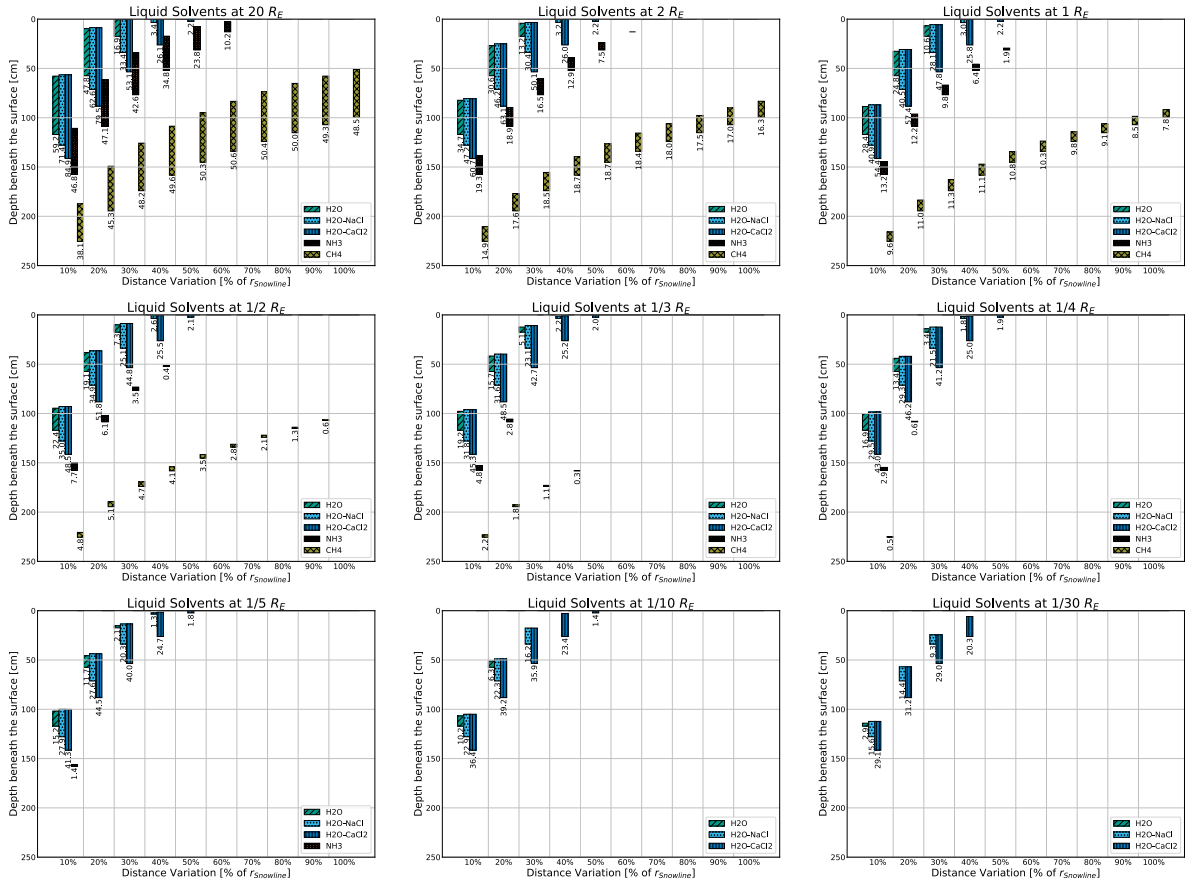


Fig. F.2:

F.1 Simulation of the rocky freshwater model with a standard day-and-night cycle (same as Fig. 4).

F.2 Simulation of the rocky freshwater model with a continuous “day” as if tidally locked.

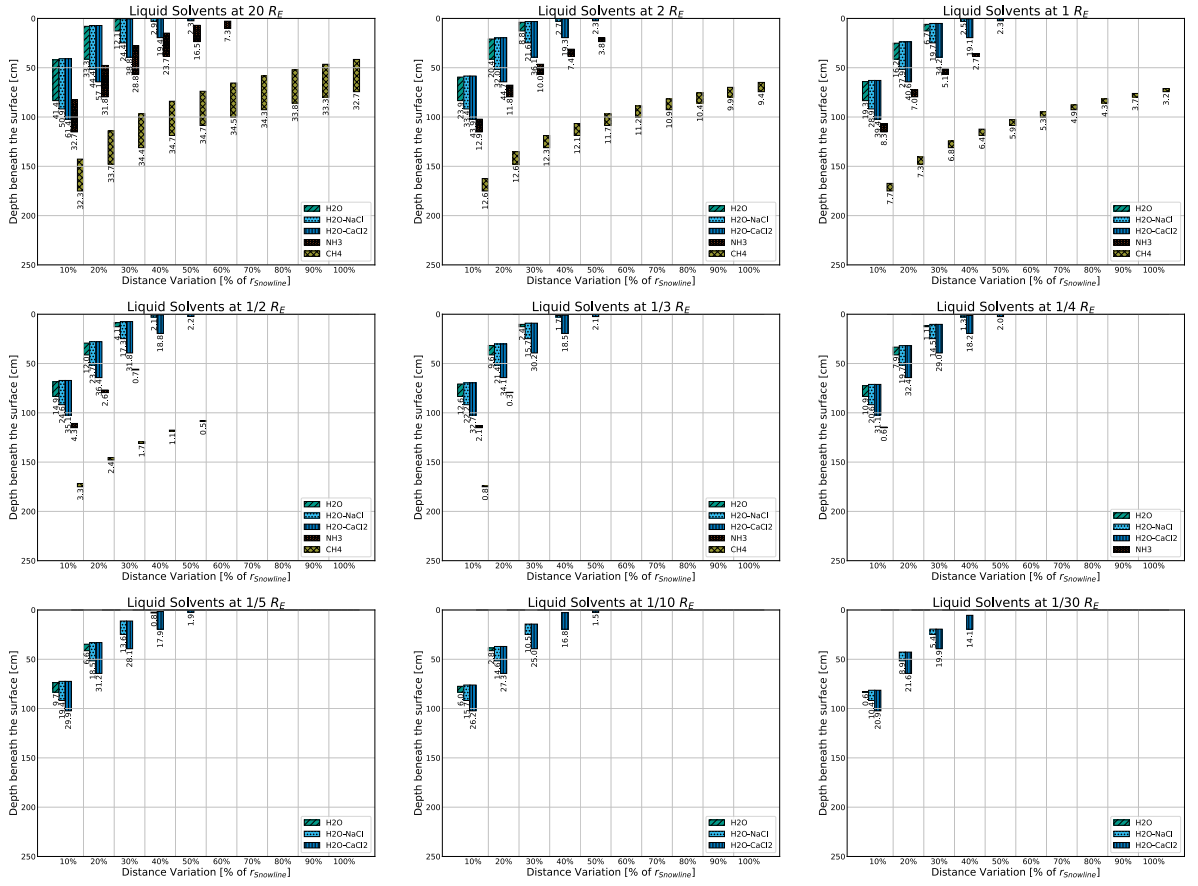


Fig. F.3:

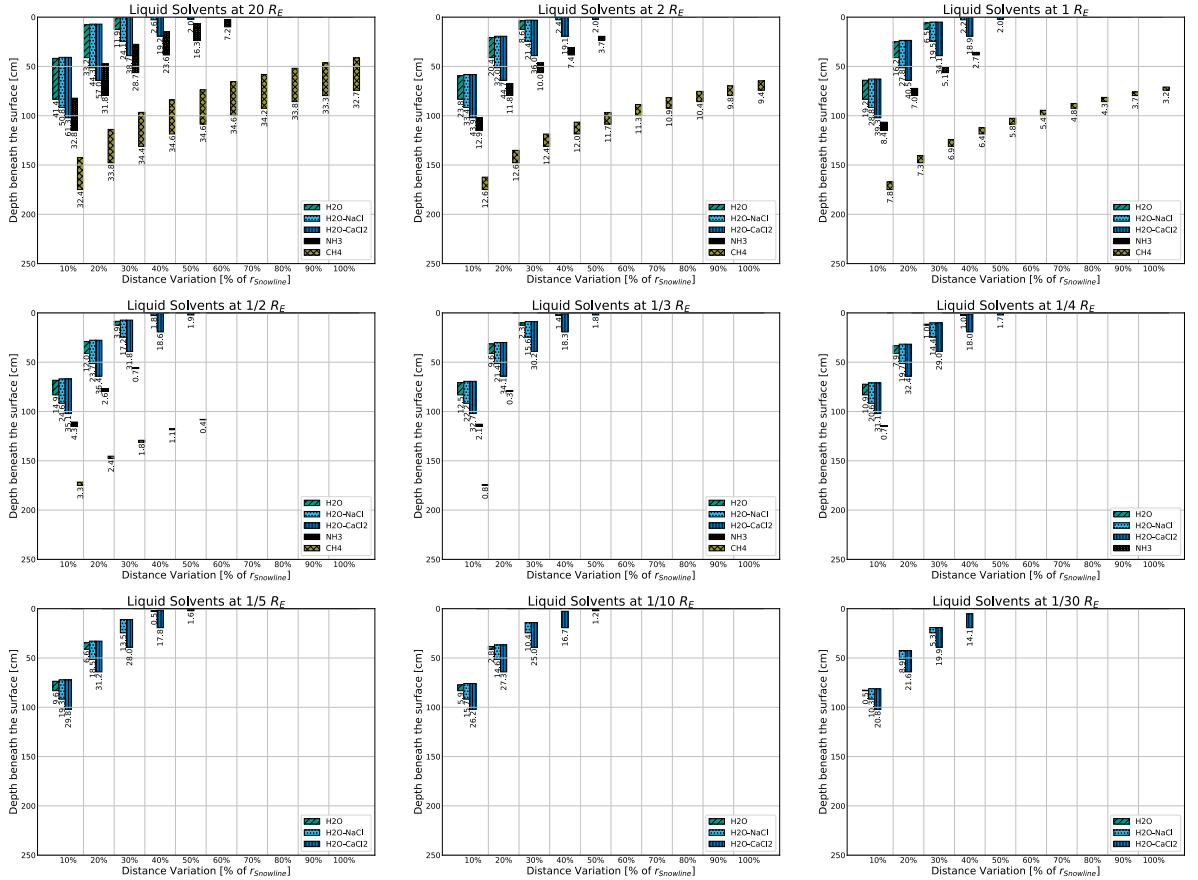
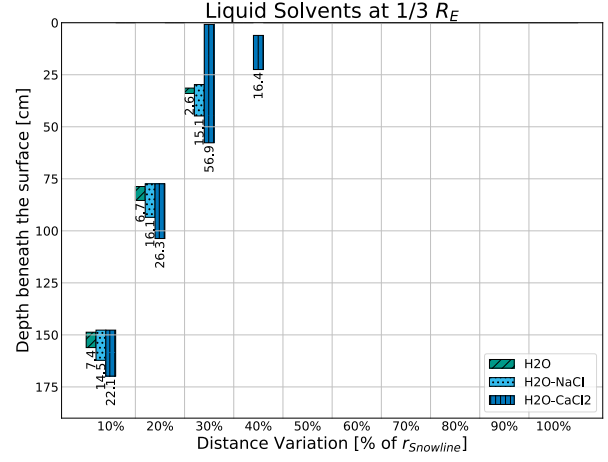
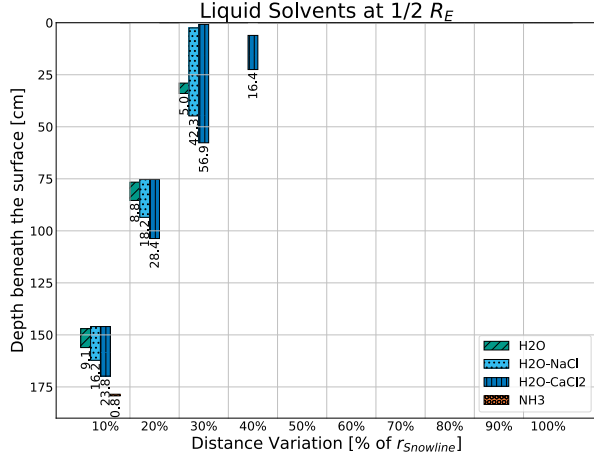


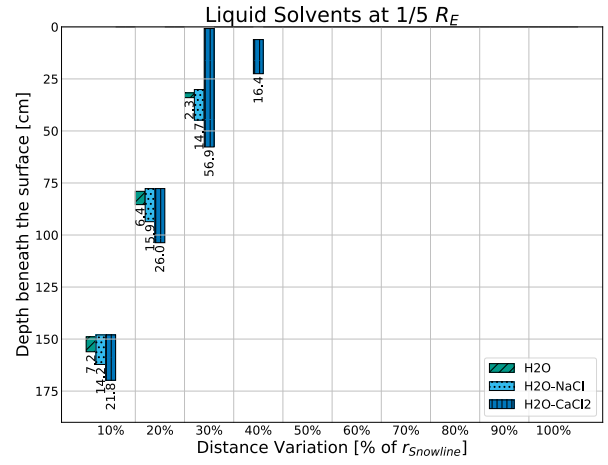
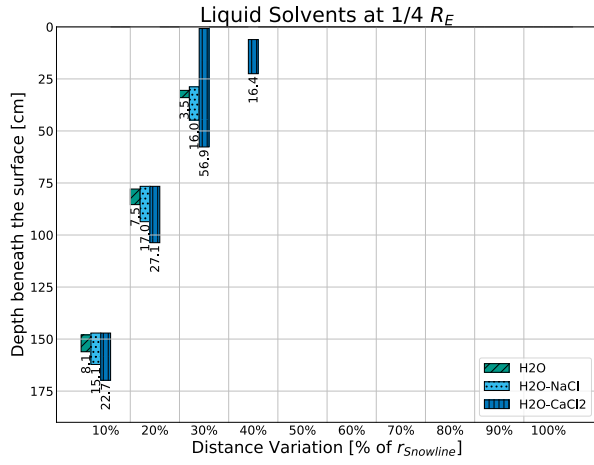
Fig. F.4:

F.3 Simulation with input coming from a single, weak source (NGC 3516), $r_{\text{snow}} = 2.95 pc$.
 F.4 Simulation with input coming from a single, strong source (Mrk 876), $r_{\text{snow}} = 14.92 pc$.

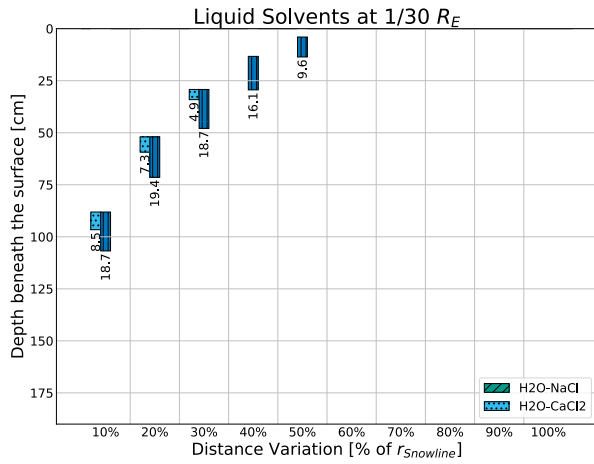
a) Ganymede



b) Europa



c) 4 Vesta



d) 511 Davida

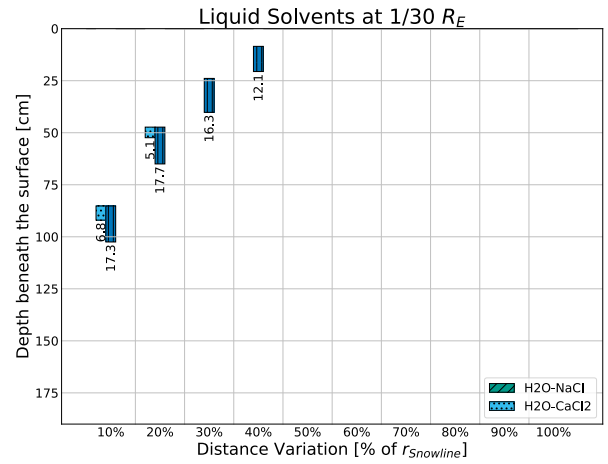


Fig. F.5: Comparisons between different approximations of smaller bodies with sizes and densities close to their real-life counterparts, with crust densities $\rho_{surface}$ as seen in Table 2. a) Jupiter's moon Ganymede ($\rho_{body} = 1.936 \frac{g}{cm^3}$) shown for sizes of $\frac{1}{2}$ & $\frac{1}{3} R_{earth}$, calculated using an icy crust. b) Jupiter's moon Europa ($\rho_{body} = 3.014 \frac{g}{cm^3}$) shown for sizes of $\frac{1}{4}$ & $\frac{1}{5} R_{earth}$, calculated using an icy crust. c) Asteroid 4 Vesta ($\rho_{body} = 3.58 \frac{g}{cm^3}$) shown for a size of $\frac{1}{30} R_{earth}$, calculated using a rocky, freshwater crust. d) Asteroid 511 Davida ($\rho_{body} = 2.48 \frac{g}{cm^3}$) shown for a size of $\frac{1}{30} R_{earth}$, calculated using a rocky, freshwater crust with modified density $\rho_{surface} = \rho_{body}$.

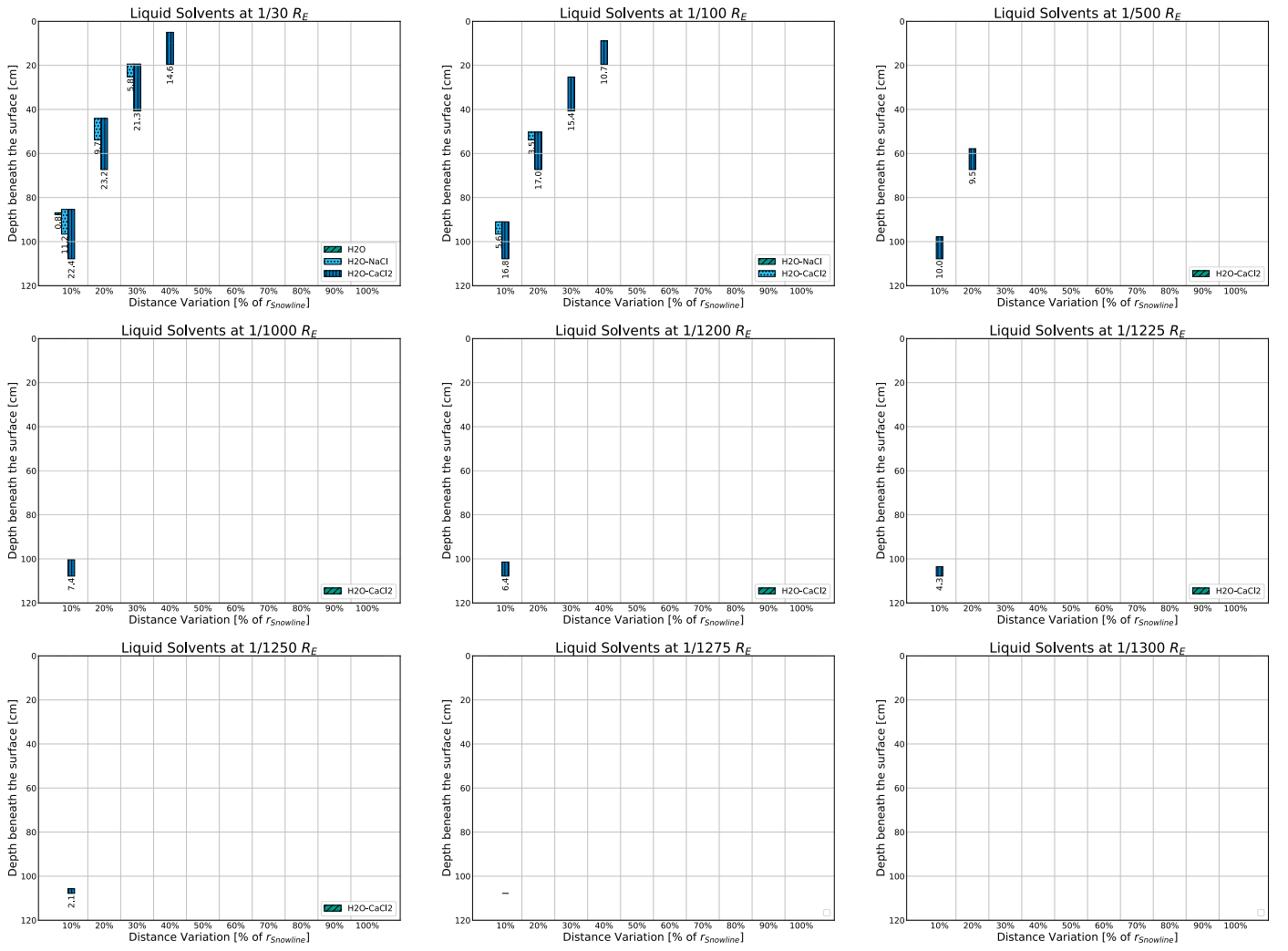


Fig. F.6: Liquid layers on very small bodies using the standard rocky, freshwater model ($\rho_{\text{surface}} = 2.2765 \frac{g}{\text{cm}^3}$, $\rho_{\text{body}} = 5.51 \frac{g}{\text{cm}^3}$). On distances very close to the source, both forms saltwater can be liquid on bodies as small as $\frac{1}{100} R_{\text{earth}}$, with CaCl_2 -saltwater even being liquid on bodies as small as $\frac{1}{1250} R_{\text{earth}}$.